

A Spectral Aging Model for the *Meteosat-7* Visible Band

I. DECOSTER

Royal Meteorological Institute of Belgium, and Vrije Universiteit Brussel, Brussels, Belgium

N. CLERBAUX, E. BAUDREZ, S. DEWITTE, A. IPE, S. NEVENS, AND A. VELAZQUEZ BLAZQUEZ

Royal Meteorological Institute of Belgium, Brussels, Belgium

J. CORNELIS

Vrije Universiteit Brussel, Brussels, Belgium

(Manuscript received 21 June 2012, in final form 3 October 2012)

ABSTRACT

For more than 30 years, the *Meteosat* satellites have been in a geostationary orbit around the earth. Because of the high temporal frequency of the data and the long time period, this database is an excellent candidate for fundamental climate data records (FCDRs). One of the prerequisites to create FCDRs is an accurate and stable calibration over the full data period. Because of the presence of contamination on the instrument in space, a degradation of the visible band of the instruments has been observed. Previous work on the *Meteosat* First Generation satellites, together with results from other spaceborne instruments, led to the idea that there is a spectral component to this degradation. This paper describes the model that was created to correct the *Meteosat-7* visible (VIS) channel for these spectral aging effects. The model assumes an exponential temporal decay for the gray part of the degradation and a linear temporal decay for the wavelength-dependent part. The effect of these two parts of the model is tuned according to three parameters; 253 clear-sky stable earth targets with different surface types are used together with deep convective cloud measurements to fit these parameters. The validation of the model leads to an overall stability of the *Meteosat-7* reflected solar radiation data record of about $0.66 \text{ W m}^{-2} \text{ decade}^{-1}$.

1. Introduction

One of the primary goals of satellites in the twentieth century was to observe weather, ocean, and land for forecasting purposes (Szekielda 1988). When the data records became sufficiently long, the usefulness of these satellites for climatological studies was recognized. This led to the creation of the European Organisation for the Exploitation of Meteorological Satellites (EUMETSAT) Climate Monitoring Satellite Application Facility (CM SAF) in 1999. From the satellite data, fundamental climate data records (FCDRs) were generated. These are time series that cover different instruments and have been extensively tested and calibrated to ensure consistency over the entire record (WMO 2006). Geophysical variables

[essential climate variables (ECVs)] such as cloud properties, precipitation, ozone, albedo, etc., were derived from these FCDRs, forming thematic climate data records (TCDRs). Stability requirements for such TCDRs are very strict. For example, the Global Climate Observing System (GCOS) requires a stability of $0.2 \text{ W m}^{-2} \text{ decade}^{-1}$ for the top-of-atmosphere earth radiation budget (WMO 2006).

These requirements are, however, usually not met using the original data. Postprocessing and intercalibrations are done to meet the criteria. An example of this is the work done by Yang et al. (2011), who demonstrate the impact and importance of the Special Sensor Microwave Imager (SSM/I) intersensor calibration for the improved FCDRs and TCDRs. Satellites in geostationary orbit provide information on a fixed viewing geometry throughout the whole day, which allows the creation of quite accurate and stable FCDRs and TCDRs.

The *Meteosat* First Generation (MFG) program consists of seven geostationary satellites, *Meteosat-1* through

Corresponding author address: I. Decoster, Royal Meteorological Institute of Belgium, Ringlaan 3 Avenue Circulaire, B-1180 Brussels, Belgium.
E-mail: ilse.decoster@meteo.be

Meteosat-7, which have been developed by the European Space Agency (ESA) and since 1986 have been operated by EUMETSAT. These instruments were operational at 0° longitude from December 1977 until June 2006, with a gap of 21 months when *Meteosat-1* failed and *Meteosat-2* was not yet launched. Every 30 min, the *Meteosat* Visible and Infrared Imager (MVIRI)—the main payload of these satellites—scanned the full earth disc in three spectral bands: the visible (VIS, 0.4–1.1 μm), the water vapor (WV, 5.7–7.1 μm), and the infrared (IR, 10.5–12.5 μm) bands.

As the MFG satellites were not designed for climatological use, attempts to create FCDRs from the 25 years of data are still ongoing. As a first step toward the generation of FCDRs, a consistent calibration is needed. For the WV and IR channels, vicarious calibrations have been derived by van de Berg et al. (1995), Gube et al. (1996), and Tjemkes et al. (2001). Koepke (1982), Kriebel and Amann (1993), Moulin et al. (1996), Lefèvre et al. (2000), and Rigollier et al. (2002) developed vicarious calibrations for the VIS channel using the known earth targets such as deserts, oceans, or clouds, whereas Brooks et al. (1984), Sohn et al. (2000), and Doelling et al. (2004a) made use of satellite inter-calibrations. Recently, the Global Space-Based Inter-Calibration System (GSICS) has been set up to ensure consistent calibration among space-based observations worldwide for climate monitoring, weather forecasting, and environmental applications (Goldberg et al. 2011). Although GSICS recognizes the interest of the MFG VIS observations, at the moment the main effort is put into calibrating the IR bands.

Degradation of the MFG VIS band

In preparation of the *Meteosat* Second Generation (MSG) satellites, EUMETSAT developed a state-of-the-art calibration method for the VIS bands of the Spinning Enhanced Visible and Infrared Imager (SEVIRI), called the SEVIRI Solar Channel Calibration (SSCC) method, which is based on radiative transfer model computations over desert and ocean targets with known spectral reflectance (Govaerts et al. 2001). The method was also applied to the MFG VIS archive (Govaerts et al. 2004) and proved to be successful in increasing the accuracy of the initial vicarious calibration. The full archive has been reprocessed to derive the official calibration, which is now published on the EUMETSAT website as a calibration coefficient at launch and a linear temporal decrease of the sensitivity due to degradation of the instrument. However, validation of this calibration method provided evidence (i) that an in-flight change of the spectral response occurred and that in particular the sensitivity decreased more at short visible wavelengths than at long, and

(ii) that there seems to be a saturation of the calibration curve (Govaerts et al. 2004).

When instruments are in space, they suffer from outgassing. This means that lightweight molecules coming from moisture, lubricants, adhesives, etc., become volatile under the vacuum conditions in spacecrafts (Frink et al. 1992; Tribble et al. 1996). This volatile material can simply condense or, when exposed to solar ultraviolet (UV) radiation, be photodeposited onto the surface of the mirrors, decreasing their reflectance. On top of that, the high-energy radiation from the sun also seems to polymerize the deposited material and thus change its optical properties, so that it absorbs more radiation in the shorter wavelengths (UV and blue VIS) than in the longer (red VIS and near IR).

This effect was reported by Matthews et al. (2005) for the Clouds and the Earth's Radiant Energy System (CERES) instruments (Wielicki et al. 1996), where different drifts were measured for clear-sky ocean scenes than for the other scenes. Hints of this spectral degradation are also visible in the data of the Geostationary Earth Radiation Budget (GERB) instrument on board the MSG satellites (N. Clerbaux 2010, personal communication). More proof was given by Delwart et al. (2006), who reported that for the Medium Resolution Imaging Spectrometer (MERIS) on board the *Environmental Satellite (Envisat)*, a stronger modification of the spectral response was needed over time for the blue end of the spectrum than for the red end. Also, the Moderate Resolution Imaging Spectroradiometer (MODIS) and the Sea-Viewing Wide Field-of-View Sensor (SeaWiFS) narrowband instruments suffer from a spectral on-orbit degradation. Xiong et al. (2009) report a higher degradation rate for the blue channels of these instruments than for the ones with a larger central wavelength. For narrowband detectors, however, it is sufficient to change the calibration coefficient for each channel independently, as the channels are small enough for the degradation to stay constant over its spectral range.

To correct the VIS channels of the MFG satellites for this spectral degradation, a semiempirical model is proposed here, without, however, the possibility of giving a full physical justification. The reason for this is that during the whole MFG history, real physical modeling of the degradation of the MVIRI instruments has never been carried out because of a lack of knowledge of the instrument characteristics and their behavior in space. It is worth noticing that these instruments had already been designed by 1970, and that they have only been characterized with the accuracy permitted at that time. In the model that is given in section 2, the calibration coefficient is kept constant, but the spectral response curve is allowed to vary in time to be able to correct for the spectral

aging effects. The methodology of how the model is applied to the *Meteosat-7* data is explained in section 3. Section 4 shows the results of the correction. The different validation methods of the model and the comparison with the EUMETSAT model are given in section 5. The conclusions and future applications for the corrected data are presented in section 6.

2. Aging model

As mentioned above, the temporal decrease in reflectance that was observed for MVIRI was adjusted by EUMETSAT by changing the calibration coefficient in time (Govaerts et al. 2004). As this allows only an overall wavelength-independent correction, and, as there is a spectral-dependent character to the degradation process of MVIRI, this spectral component needs to be included in the correction. This is achieved here by creating a model that lets the spectral response $\phi(\lambda)$ change in time. The first part of this model covers the gray degradation, that is, the wavelength-independent part. Based on the ideas from Xiong et al. (2009), Matthews et al. (2005), and the NASA study performed by Stewart et al. (1990), an exponential degradation is used. This gray part of the model is based on two parameters: α , the decay rate of gray degradation, and β , the asymptotic sensitivity when $t \rightarrow \infty$, and it takes the form of $e^{-\alpha t} + \beta(1 - e^{-\alpha t})$. A physical interpretation would be that $1 - e^{-\alpha t}$ is the fraction of the instrument that is contaminated and $e^{-\alpha t}$ is the fraction of the instrument that is not yet contaminated.¹ Then β can be seen as the sensitivity of the damaged part, and this way the sensitivity of the full instrument goes to β when $t \rightarrow \infty$.

For the spectral part of the degradation model, different possibilities were investigated. In the case of CERES, Matthews et al. (2005) proposed a model that is an exponential function of wavelength. This idea is based on the fact that atomic oxygen is a major source of contamination for polar-orbiting instruments (Dooling and Finckenor 1999). As all instruments in the *Meteosat* Program occupy a geostationary orbit instead of a polar one, the CERES model did not provide good enough results for the MFG instruments. Instead, a linear function of time and wavelength was chosen with γ as the temporal decay rate of spectral degradation. The full model of the on-orbit spectral response $\phi(\lambda, t)$ at time t then takes the following form:

¹ One could say that the degradation of the instrument is affected by both the degradation of the mirror and the detector. In which case, $e^{-\alpha t}$ would be written as $e^{-\alpha_1 t}$; $e^{-\alpha_2 t} = e^{-(\alpha_1 + \alpha_2)t} = e^{-\alpha t}$, where α_1 is the decay rate of degradation of the mirror and α_2 is the decay rate of degradation of the detector.

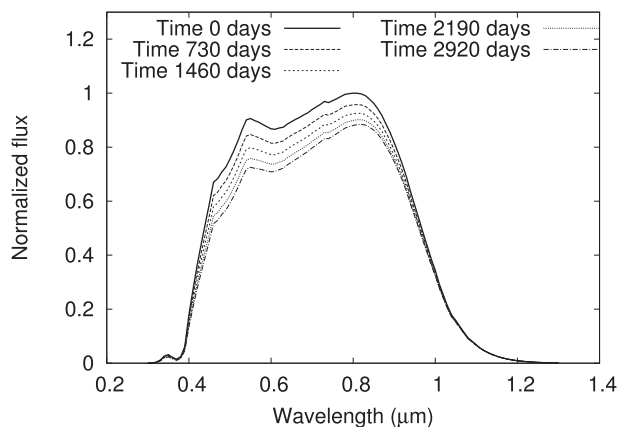


FIG. 1. Normalized spectral response functions of *Meteosat-7* VIS channel at launch, after 730 days (2 yr), 1460 days (4 yr), 2190 days (6 yr), and 2920 days (8 yr). Following the model, there is both a gray exponential degradation ($\alpha = 1.1643 \text{ decade}^{-1}$, $\beta = 0.7489$) and a wavelength-dependent linear degradation ($\gamma = 0.4745 \mu\text{m}^{-1} \text{ decade}^{-1}$) present in these response curves.

$$\phi(\lambda, t) = \phi(\lambda, 0)[e^{-\alpha t} + \beta(1 - e^{-\alpha t})][1 + \gamma t(\lambda - \lambda_0)] \quad (1)$$

with α , β , and γ as the model parameters; $\phi(\lambda, 0)$ is the spectral response function at launch; and λ_0 is the central wavelength of the VIS response curve at launch. Figure 1 shows the original spectral response function $\phi(\lambda, 0)$ of *Meteosat-7* together with the corrected response curves $\phi(\lambda, t)$ with $t = 2, 4, 6,$ and 8 yr following the above-mentioned model (the parameters are given in Table 2). The wavelength-dependency is visible when comparing the curves at short and long wavelengths: at longer wavelengths, the curves decrease less in time than at shorter wavelengths.

Apart from time and wavelength, the model is also strongly dependent on the spectral response curve, as it was measured prior to launch. For *Meteosat-7*, the original response curve was characterized quite accurately,² while for the older satellites it was not always the case.

3. Methodology

The explanation of the methodology below is based on the *Meteosat-7* data. The same methods, however, can be applied on the data of any of the other MFG instruments. In this work only one image of 5000×5000 pixels is used per day. For the majority of the images, this is the one at 1200 UTC. When this image is not available or if the quality is not good, then the one at

² The original spectral response curve was cut off at $\lambda = 1 \mu\text{m}$. The idea of Govaerts et al. (2004) to extend the response curve for $\lambda > 1 \mu\text{m}$ was adopted in this work.

1100 UTC is used; otherwise, the image at 1300 UTC is selected. When it is not possible to use any of these three images, the day is skipped. The data period at 0° longitude used is from 3 June 1998 to 11 June 2006.

a. From digital count to reflectance ratio

All images are first transformed from digital counts to radiance L , defined as

$$L = C_f(v - O)$$

with v as the original value in digital counts and C_f and O as the calibration coefficient and offset value, respectively. The latter two stay fixed throughout this work at the values at launch calculated by Govaerts et al. (2004) for *Meteosat-7*: $C_f = 0.9184 \text{ W m}^{-2} \text{ sr}^{-1} \text{ DC}^{-1}$ and $O = 4.84 \text{ DC}$.³ This radiance is called filtered or narrowband (NB) radiance, as it was filtered by the instrument's spectral response $\phi(\lambda)$ as it went through (optics throughput and detector response), that is,

$$L = \int_{\text{VIS}} L(\lambda)\phi(\lambda) d\lambda \quad (2)$$

where $L(\lambda)$ is the spectral radiance at wavelength λ coming into the instrument. The integration covers the whole MFG visible band wavelength range.

Next, this narrowband radiance L is transformed into narrowband reflectance ρ as follows:

$$\rho = \frac{L}{\frac{\text{FSI} \cos(\theta_0)}{\pi d^2}} \quad (3)$$

where θ_0 is the solar zenith angle, d is the distance between the sun and the earth in astronomical units (AU), and FSI is the filtered solar irradiance given by EUMETSAT on their webpage (FSI = 690.8 W m⁻²).⁴

The filtered reflectance is then transformed into unfiltered broadband (BB) reflectance following a linear relation between both, as shown:

$$\rho_{\text{BB}} = a + b\rho. \quad (4)$$

³ The calibration and offset coefficients can be found on the EUMETSAT webpage as version 07.07.01. The calibration coefficient is given as a constant value. The offset, however, is given for different smaller periods, and the fixed value used here is the time average of all of these periods over the full *Meteosat-7* time range.

⁴ The FSI was computed using the solar spectrum as measured by the Atmospheric Laboratory for Applications and Science (ATLAS).

To find the coefficients a and b , radiative transfer simulations are done for the spectral radiance $L(\lambda)$ for different surface types. The spectral signatures for the simulations are obtained from Clerbaux et al. (2008) for 750 different scenes. The simulations are made using the Santa Barbara DISORT (discrete ordinate radiative transfer) atmospheric radiative transfer (SBDART) model (Ricchiazzi et al. 1998). This is carried out for a large set of surface types characterized by a mixture of one or several surface reflectance models from the Advanced Spaceborne Thermal Emission and Reflection Radiometer (ASTER) library (Baldrige et al. 2009), and for different types of aerosols and cloudiness. The simulations cover all possible solar and viewing geometries, with an angular resolution of 10° for the solar zenith angle θ_0 and relative azimuth angle ψ , and 5° for the viewing zenith angle θ . The simulations are done with a sufficiently fine spectral resolution to create simulated narrowband [Eq. (2)] and broadband radiances [Eq. (6)]. Using the modeled spectral response curve $\phi(\lambda, t)$ from Eq. (1), the simulated narrowband radiance becomes

$$L = \int_{\text{VIS}} L(\lambda)\phi(\lambda, 0)[e^{-\alpha t} + \beta(1 - e^{-\alpha t})][1 + \gamma t(\lambda - \lambda_0)] d\lambda = [e^{-\alpha t} + \beta(1 - e^{-\alpha t})](L^0 + \gamma t L') \quad (5)$$

with

$$L_0 = \int_{\text{VIS}} L(\lambda)\phi(\lambda, 0) d\lambda$$

$$L' = \int_{\text{VIS}} L(\lambda)\phi(\lambda, 0)(\lambda - \lambda_0) d\lambda$$

and the simulated broadband radiance is computed as

$$L_{\text{BB}} = \int_{0-2\mu\text{m}} L(\lambda) d\lambda. \quad (6)$$

After both NB- and BB-simulated radiances are converted into reflectance using Eq. (3) with the same constant value for FSI, the coefficients a and b are fitted for each time t and each surface type through Eq. (4). Figure 2 shows a sample of simulated NB and BB reflectances for different surface types at time $t = 0$ and with $\theta_0 = 50^\circ$, $\theta = 30^\circ$, and $\psi = 50^\circ$. From this figure it is clear that a linear relation exists between narrowband and broadband reflectance, and a linear fit can be done. The coefficients a and b are then used through Eq. (4) to convert the observed filtered reflectance into unfiltered reflectance. This conversion is needed to obtain a parameter independent of degradation of the spectral response. The narrowband reflectance ρ is filter dependent,

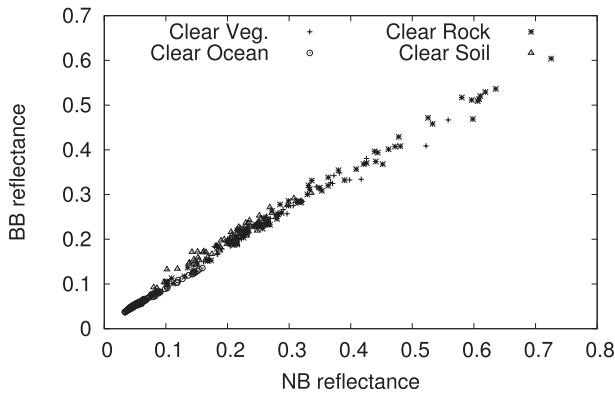


FIG. 2. Simulated NB and BB reflectances for different surface types and with angles $\theta_0 = 50^\circ$, $\theta = 30^\circ$, and $\psi = 50^\circ$. The BB reflectance values are plotted here as a function of the NB reflectances.

and thus aging dependent, whereas broadband reflectance is computed using a flat normalized spectral response function, so that there is no dependence on the *Meteosat-7* filter. This means that it should be possible to find model parameters that will lead to broadband time series with a slope close to zero.

As a final step, the unfiltered (broadband) reflectance values are divided by a modeled anisotropy factor (R) and albedo (Alb) to correct for the difference in sun-earth-satellite geometry, and for the difference in reflectance for different surface types. For clear-sky sites, R and Alb have been empirically estimated by Loeb et al. (2003) using data of the CERES instrument on the Tropical Rainfall Measuring Mission (TRMM) satellite (Kummerow et al. 1998).⁵ As the shortwave spectral response of the CERES instrument is broader than the one of MFG, the cloudy R and Alb contain the effects of the deep ice and water absorption bands between 1 and 2 μm . For this reason the anisotropy and albedo values for deep convective clouds are not taken from Loeb et al. (2003). Instead, they are modeled with the radiative transfer program libRadtran (Mayer and Kylling 2005) using the Key et al. (2002) parameterization with the solid column crystal habit. The result of the division of measured broadband by modeled broadband is called the reflectance ratio r , written as

$$r = \frac{\rho_{\text{BB}}}{R(\theta_0, \theta, \psi)\text{Alb}(\theta_0)} \quad (7)$$

in which the dependency of r on the angles θ_0 , θ , and ψ is expected to be removed, and the r value should be close to 1.

⁵ The availability of these broadband CERES models is also the reason why the NB-to-BB correction is done for *Meteosat* and why no other stable conversion is used.

b. Selection of clear-sky targets

As the model depends on time and wavelength, reflectance ratio time series for targets with different spectral characteristics could be used to fit the model parameters α , β , and γ for each instrument separately. These targets are chosen to be the most stable sites in the *Meteosat* field of view⁶ (FOV) in order to have as little noise as possible on the time series. To have a wide variety in reflectance ratio values, different surface types are selected using both cloudy and clear-sky targets. The next two sections explain how the target selection is done.

To find clear-sky targets, clear-sky images are created every 10 days using a pixel-to-pixel analysis of a series of 30 reflectance ratio images before and 30 reflectance ratio images after the original one, following the method of Ipe et al. (2003). As an example, Figs. 3a and 3b show an original image expressed in reflectance ratio r (dated 14 March 2002) and its clear-sky version. To reduce the effect of spatial variability at the pixel level, each clear-sky image is transformed into a so-called local mean image (see Fig. 3c). This means that each clear-sky pixel is replaced by the average value in the image of all pixels in a box of 25×25 around this one.

As the decrease in signal of the satellite can be approximated to the first order by a linear function, a linear fit in time is computed over the whole *Meteosat-7* time range for each individual pixel in these local mean images. Based on this, the variance, defined as the quadratic deviation to each fitting line, is computed and stored in a so-called variance image. Here each pixel contains the variance of the linear fit of this pixel over the whole time range. In the same way, the mean image is computed as the image where each pixel is the average of the pixels with the same position over the whole time range of images. In a next step, the pixel-to-pixel ratio of the variance to the mean is taken in order to normalize the variance. This variance-to-mean ratio image is shown in Fig. 3d. The most stable sites (with respect to the linear fit) are then the pixels with the lowest normalized variance.

The last requirement on these sites is that no two sites can be located closer than 50 pixels, that is, each site is the local minimum of variance-to-mean value ratio in a box of 51×51 pixels. This ensures that two adjacent sites come from geographic regions that are different enough, and that the number of sites stays limited. Figure 4 shows the locations of the final 253 clear-sky targets in the *Meteosat* FOV.

⁶ The *Meteosat* field of view is the part of the earth that is observed from the geostationary orbit of the *Meteosats* at their nominal position of 0° longitude.

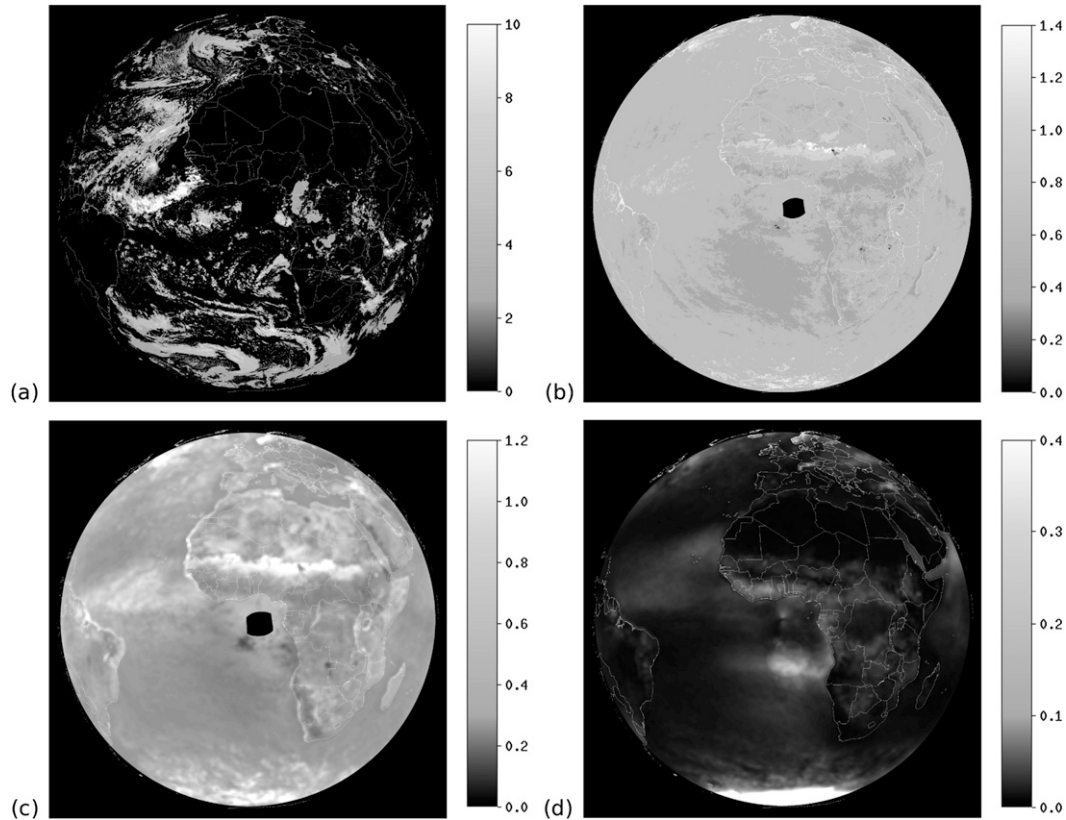


FIG. 3. The *Meteosat-7* VIS image of 14 Mar 2002 as (a) the original reflectance ratio image, (b) the clear-sky reflectance ratio image, (c) the local mean reflectance ratio image, and (d) the variance-to-mean ratio image of the full *Meteosat-7* data range. The black spot in the center of (a)–(c) and the white spot in (d) are due to data removed because of sun glint.

c. Selection of cloudy targets

The most stable cloudy pixels are the ones that contain deep convective clouds, as these are the clouds with the highest and most stable reflectance values, due to the ice crystals at the top (Vermote and Kaufman 1995; Doelling et al. 2004b). To select cloudy targets, the original images that still contain clouds are used. Because clouds move, different pixels are used as a target in each frame.

As a first step, the original image is replaced by a local mean image in the same way as described in section 3b. Here, however, each original pixel is replaced by the average value of a box of 9×9 pixels. These boxes are smaller because they are mainly used to remove the effects of very small clouds and to smooth out the borders of the biggest clouds. The deep convective cloud scenes are then found as the local maxima of boxes of 151×151 pixels. These boxes are larger than the boxes used for the clear-sky target selection process because convective clouds can be large, and we do not want to select different scenes from the same convective cloud.

d. From targets to time series

For all of these clear-sky and cloudy targets, reflectance ratio time series are constructed for the full *Meteosat-7* time range. Before they are used to find the best model parameters, a seasonal correction and surface-type averaging are performed on the time series as follows.

First, residual small seasonal effects are corrected for by subtracting the mean annual cycle from the reflectance ratio value time series [Qian et al. (2011)]. An example of this is shown in Fig. 5, where the time series of a site with high seasonal variation is plotted before and after the seasonal correction.

Next, the 253 clear-sky time series are averaged according to five different surface types (ocean, dark vegetation, bright vegetation, dark desert, and bright desert).⁷ First, this grouping is done to decrease the number of

⁷ As there are almost no snow pixels in the *Meteosat* FOV, this surface type was not used at all in this work. Furthermore, the snow spectrum in the visible band is very similar to the convective cloud spectrum (see Dozier 1989).

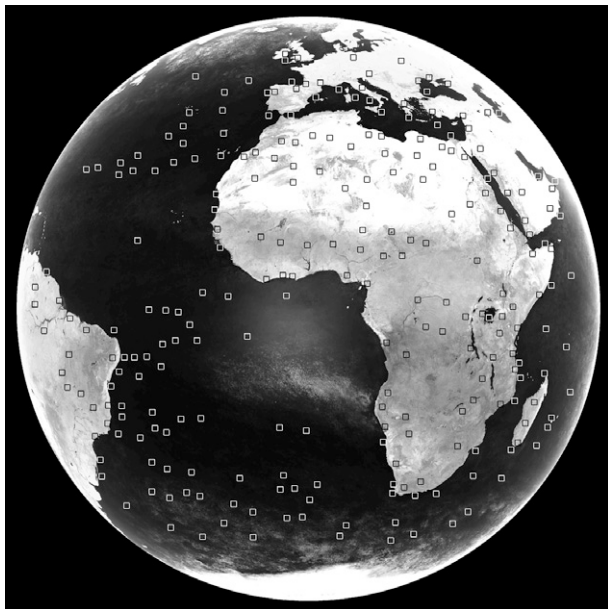


FIG. 4. Position of the 253 clear-sky targets used in this work.

time series to check while still keeping information about the whole *Meteosat* FOV. Second, it is also not possible to ensure that each individual target is stable; however, grouped together, the less stable time series are averaged out. Third and most importantly, it seems that the aging effect is stronger for scene types with a strong component in the blue part of the visible spectrum. By selecting the sites with the same surface type, similar spectral characteristics are being grouped together and targets with distinct spectral properties can be compared with each other. On the cloudy side, only one time series is created. This is done by selecting, for each individual image, the five scenes with the highest reflectance ratio values and averaging these. Also, a time averaging over 10 days is done for the cloudy time series to have the same temporal resolution as for the clear-sky time series.

Together, this results in six time series, which are plotted in Fig. 6a. The first thing to notice in this figure is the slight difference in degradation rate for the different time series. The dark and bright vegetation decrease $1.2\%–1.4\% \text{ yr}^{-1}$, while the dark and bright desert decrease $1.5\%–1.7\% \text{ yr}^{-1}$. The ocean time series decrease about $1.8\% \text{ yr}^{-1}$ and the convective cloud time series $1.9\% \text{ yr}^{-1}$. The exact numerical value for the slope of each time series is given in column 4 of Table 1. The error on each value is given by the square root of the reduced chi-square statistics χ_{red} of the fit of each time series, as shown:

$$\chi_{\text{red}} = \sqrt{\frac{\text{SSR}}{\text{NDF}}} \quad (8)$$

where SSR is the sum of squares of residuals and NDF is the number of degrees of freedom. The number of

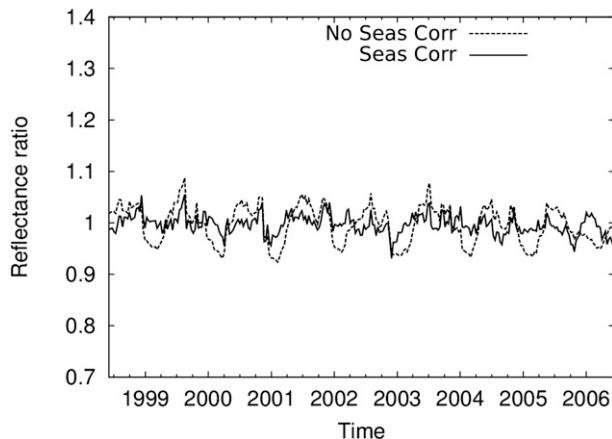


FIG. 5. Time series for site with coordinates (2288, 2222) before and after the seasonal correction. This target is one with high seasonal variation, where there was still a small seasonal effect visible in the time series.

degrees of freedom is calculated as the number of points in the time series minus the number of parameters in the fit. As a linear fit is done through the time series, the number of parameters in the fit is equal to 2. As the ocean spectrum has a strong peak in the blue part of the visible wavelength, and the spectrum of the convective clouds also covers the full blue visible wavelengths (the absorption of these ice clouds increases with increasing wavelengths), this slightly stronger decrease in time for the convective clouds and ocean time series corroborates the wavelength dependence of the degradation process of *Meteosat-7*. A stronger degradation, however, is expected for the ocean than for the convective clouds just because of this strong peak in the blue visible wavelengths. Even though this is not the case for the broadband reflectance ratio time series, it is the case for the narrowband version of these time series (where the narrowband-to-broadband conversion has not been done). The fifth column of Table 1 shows that, indeed, the ocean time series decrease stronger than the convective cloud time series when expressed in NB reflectance ratio instead of BB reflectance ratio. The reason for this is to be found in the NB-to-BB conversion, as shown:

$$\rho_{\text{BB}} = a + b\rho_{\text{NB}}$$

and can be explained as follows. Expressing this conversion in reflectance ratio, using $\tilde{\rho} = R(\theta_0, \theta, \psi)\text{Alb}(\theta_0)$ in Eq. (7) leads to

$$r_{\text{BB}}\tilde{\rho}_{\text{BB}} = a + br_{\text{NB}}\tilde{\rho}_{\text{NB}}.$$

Taking the partial derivative of this equation to time results in the slope of the reflectance ratio time series, defined as

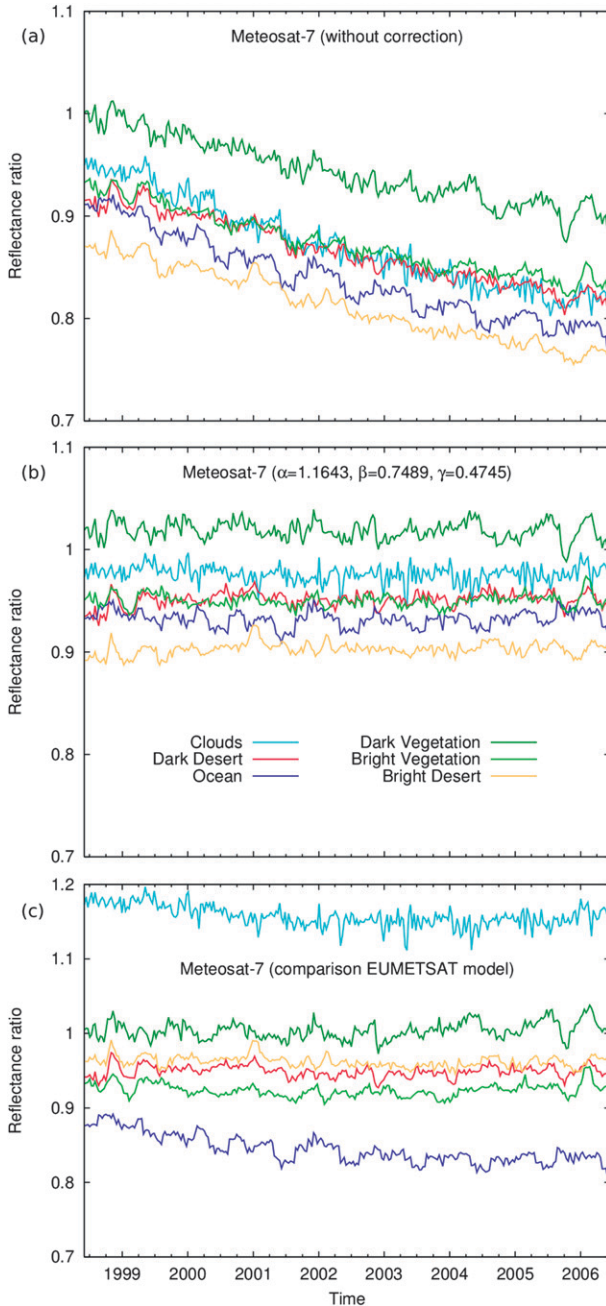


FIG. 6. *Meteosat-7* reflectance ratio time series for the five clear-sky and one cloudy time series with (a) the time series before the aging correction was done, (b) after they were corrected for degradation using the aging model of Eq. (1), and (c) after they were corrected using the model from Govaerts et al. (2004) as used by EUMETSAT.

$$\tilde{\rho}_{BB} \frac{\partial r_{BB}}{\partial t} = b \tilde{\rho}_{NB} \frac{\partial r_{NB}}{\partial t}.$$

The slopes are divided by the intercept to get the relative change in time, as shown:

$$\begin{aligned} \frac{\tilde{\rho}_{BB} \frac{\partial r_{BB}}{\partial t}}{r_{BB} \tilde{\rho}_{BB}} &= \frac{b \tilde{\rho}_{NB} r_{NB} \tilde{\rho}_{NB}}{a + b r_{NB} \tilde{\rho}_{NB}} \left(\frac{\partial r_{NB}}{r_{NB} \tilde{\rho}_{NB}} \right) \\ \frac{\partial r_{BB}}{r_{BB}} &= \frac{b r_{NB} \tilde{\rho}_{NB}}{a + b r_{NB} \tilde{\rho}_{NB}} \left(\frac{\partial r_{NB}}{r_{NB}} \right) \\ &= \frac{1}{1 + \frac{a}{b r_{NB} \tilde{\rho}_{NB}}} \left(\frac{\partial r_{NB}}{r_{NB}} \right) \\ &= \frac{1}{1 + \frac{a}{b \rho_{NB}}} \left(\frac{\partial r_{NB}}{r_{NB}} \right). \end{aligned}$$

Filing in typical values for the NB reflectance ρ_{NB} and the (a, b) coefficients for possible angles $\theta_0 = 30^\circ, \theta = 30^\circ$, and $\psi = 90^\circ$ leads for convective cloud time series to

$$\frac{1}{1 + \frac{a}{b \rho_{NB}}} = \frac{1}{1 + \frac{0.04}{0.9 \times 0.7}} \approx 0.94$$

and for ocean time series in

$$\frac{1}{1 + \frac{a}{b \rho_{NB}}} = \frac{1}{1 + \frac{0.014}{0.94 \times 0.1}} \approx 0.87.$$

This explains why the ratio of NB-to-BB slope is bigger for the ocean time series than for the convective cloud time series.

From Fig. 6a it can also be seen that the initial reflectance ratio values differ from 1 for five of the six time series. The reason that they differ from 1 can come from three sources. First, the spectral response at launch is never perfectly known. Second, the narrowband-to-broadband correction relies on simulations that may not perfectly represent the observed surface type. Third, the CERES TRMM angular distribution models used to convert the reflectance values to reflectance ratio are global tropical models. This means that the models for each different surface type are based on observations from that surface type from the global tropical region. The models will be good as an average over that region, but they might slightly misrepresent targets in the *Meteosat* FOV alone. The inadequacy of the CERES TRMM models in the *Meteosat* FOV has been reported for dark vegetation by Bertrand et al. (2006).

e. Minimizing variance cost function

The ultimate goal is to correct the MFG data for degradation and thus find the set of model parameters

TABLE 1. For each surface type, the number of sites used is given, the weight values used in the cost function in Eq. (9), the slope of the original time series expressed in BB reflectance ratio, the slope of the original time series expressed in NB reflectance ratio, the slope of the BB reflectance ratio time series corrected using the model of Govaerts et al. (2004), and the BB reflectance ratio time series corrected using the model from this paper. The error on each slope value is the square root of the reduced chi-square statistics χ_{red} .

Surface type	No. of sites	Weight w_i	Original BB slope (% yr ⁻¹)	Original NB slope (% yr ⁻¹)	Govaerts slope (% yr ⁻¹)	Current model slope (% yr ⁻¹)
Convective clouds	1	0.6562	-1.9090 ± 0.0230	-2.0144 ± 0.0295	-0.2689 ± 0.0263	-0.0463 ± 0.0181
Ocean	127	0.1611	-1.7900 ± 0.0222	-2.4311 ± 0.0280	-0.7562 ± 0.0238	-0.0105 ± 0.0166
Dark vegetation	22	0.0252	-1.2542 ± 0.0204	-1.6699 ± 0.0244	0.1219 ± 0.0234	-0.0605 ± 0.0190
Bright vegetation	49	0.0554	-1.3895 ± 0.0167	-1.7932 ± 0.0205	-0.0139 ± 0.0183	0.0030 ± 0.0129
Dark desert	11	0.0268	-1.5328 ± 0.0156	-1.8030 ± 0.0185	-0.0320 ± 0.0165	0.0758 ± 0.0147
Bright desert	44	0.0753	-1.6847 ± 0.0149	-1.8631 ± 0.0180	-0.1011 ± 0.0154	0.0623 ± 0.0132
Total sum-weighted average	254	1.00	-1.8176	-2.0435	-0.3044	-0.0267

(α , β , γ) that leads to time series with a slope close to zero. This is done as follows:

- 1) Simulate the spectral radiance $L(\lambda)$ for different surface types and times.
- 2) Set the model parameters (α , β , γ) to an initial value.
- 3) Calculate L and L_{BB} using Eqs. (5) and (6) with the given values for α , β , and γ .
- 4) Convert these simulated radiances into reflectances using Eq. (3).
- 5) Do the NB-to-BB conversion of Eq. (4), fitting the a and b values for these simulated reflectance values.
- 6) Use the values for a and b from this conversion to convert the observed reflectance ρ to broadband reflectance ρ_{BB} [Eq. (4)].
- 7) Transform ρ_{BB} to reflectance ratio r using Eq. (7).
- 8) Calculate the cost function

$$\sum_{i=1}^6 w_i \left\{ \frac{1}{N} \left[\sum_{j=1}^N r_{ij}^2 - \frac{\left(\sum_{j=1}^N r_{ij} \right)^2}{N} \right] \right\} \quad (9)$$

using the method of Powell (1964) and using these r values.⁸

- 9) If the cost function does not lead to the optimal solution, then the Powell method returns a new set of (α , β , γ) parameters and the routine goes back to step 3.

The weights used in the cost function for the clear-sky time series were determined using the presence of each surface type in the Meteosat FOV. For the clouds the

weight was obtained using a statistical analysis in the FOV. The values for the weights w_i are given in the third column of Table 1 for each different time series.

4. Results

The search for the set of model parameters (α , β , γ) that leads to undegraded time series was performed on the *Meteosat-7* database. The optimal solution from the cost function is given in Table 2, together with the standard deviation of each parameter. The standard deviation was computed by running the same minimization technique on 30 different subsets of 100 time series (of the 254). As the standard deviations of the parameters are all smaller than the parameter values themselves, the optimal solution is significant. The clear nonzero value for the γ parameter indicates the need for a wavelength-dependent correction of degradation.

These α , β , and γ values result in the corrected time series shown in Fig. 6b. Comparing this with Fig. 6a, one thing that can be seen is that the starting point of the six time series in Fig. 6b are slightly higher than the ones in Fig. 6a. The reason for this is that the aging correction starts at launch in September 1997 but that the dataset used to present the results in this work starts in June 1998. Apart from that, it is clear that the time series are all corrected for aging, and that they are now all quasi horizontal. The slope for each of the time series is given in column 7 of Table 1, expressed in percentage per year.

TABLE 2. The optimal solution is given for each parameter together with its standard deviation.

Parameter	Optimal solution	Standard deviation
Gray decay rate α	1.1643 decade ⁻¹	0.1606 decade ⁻¹
Asymptotic sensitivity β	0.7489	0.0161
Spectral decay rate γ	0.4745 μm^{-1} decade ⁻¹	0.0329 μm^{-1} decade ⁻¹

⁸ Index i runs over all six time series, index j over all points in the time series, w_i is the weight given to each of the six time series, N is the number of points in the time series, and r_{ij} is the reflectance ratio for time series i and time j .

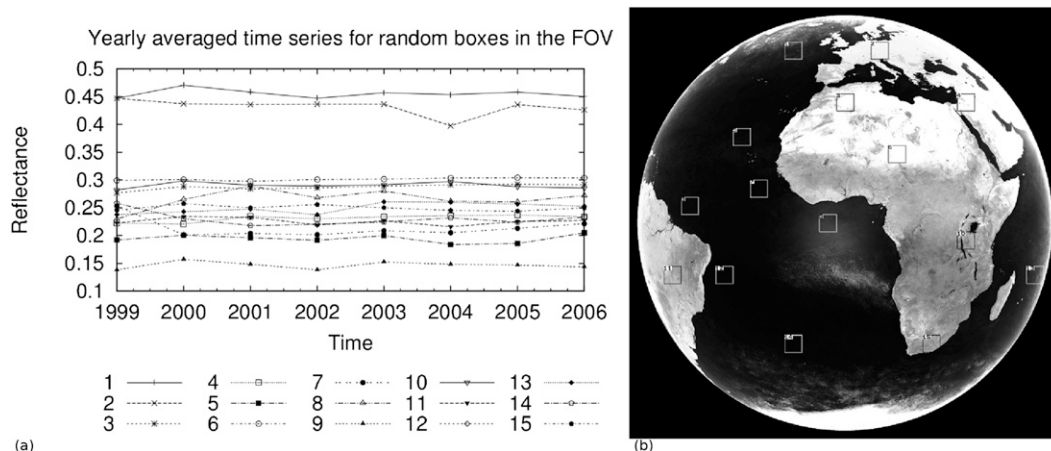


FIG. 7. Yearly averaged reflectance time series in (a) for the random selection of boxes of 200×200 pixels shown in (b) in the Meteosat FOV at 0° longitude.

The values confirm the improvement as they are now all clearly smaller than the original ones. The residual error for each individual time series is expressed as the square root of the reduced chi-square statistics χ_{red} of the fit of each time series. The resulting time-dependent spectral response curves were already shown in Fig. 1 for $t = 2, 4, 6$ and 8 yr.

5. Validation

Several different steps have been taken to validate this model. First, the model is applied to all-sky observations, where different surface types are grouped together. The result of this is shown in section 5a. A second validation is based on the dataset from the International Geosphere-Biosphere Programme (IGBP; Eidenshink and Faundeen 1994; Loveland and Belward 1997). Instead of grouping the Meteosat FOV pixels into five groups according to their surface type, the 17 classes of the IGBP dataset are used. The method and residual slopes of the time series are given in section 5b. Finally, the model explained here is compared to the model that was already in use by EUMETSAT. This comparison is shown in section 5c.

a. Regional validation

The key to the first validation is that, instead of the clear-sky and convective cloud simulations that were used for the NB-to-BB conversion, all-sky simulations are used allowing all types of clouds. These simulations are also created using the SBDART model. As before, the pixels of the original images are converted from radiance to reflectance; however, for the NB-to-BB conversion of Eq. (4), the values for a and b are now fitted on the all-sky simulations. As there are no all-sky R and Alb

values (only for strictly clear-sky or cloudy pixels), the division by the R and Alb is not done and thus the broadband reflectance values are not converted into reflectance ratio, as was done before. Filling in the values for the model parameters α, β , and γ that came out of the optimization process (see Table 2) and applying the model to all images, any time series derived from these corrected images should be corrected for aging and should thus have a slope close to zero, as long as the cloudiness does not vary too much.

To show that this is the case, the Meteosat FOV is divided into 625 boxes, each 200×200 pixels. For each box, the reflectance values are averaged and used to create time series. As each box contains 40 000 pixels, this means that different surface types are combined in each time series. To show the results, first, a few random boxes have been selected. Their position is shown in Fig. 7b on top of the Meteosat FOV. As the broadband reflectance values are not converted into reflectance ratio, the pixels are not corrected for differences in solar illumination in different seasons. To mitigate these seasonal effects, yearly averages are taken. The resulting time series are shown in Fig. 7a.

To check how flat the time series actually are, the residual slopes of the time series have been computed. This is done for the 401 of 625 boxes in the Meteosat FOV that satisfy the condition $\theta < 80^\circ$ and $\theta_0 < 80^\circ$, including the random selection of boxes from Fig. 7. The spatial distribution of the residual slopes is shown in Fig. 8a. Figure 8c gives the slopes as a function of their mean reflectance. In the latter, the error bars on the slopes are the square roots of the reduced chi-square statistics χ_{red} of the fit of each individual time series as explained in the previous section. Figure 8c shows that the slopes are all grouped around zero, with a few

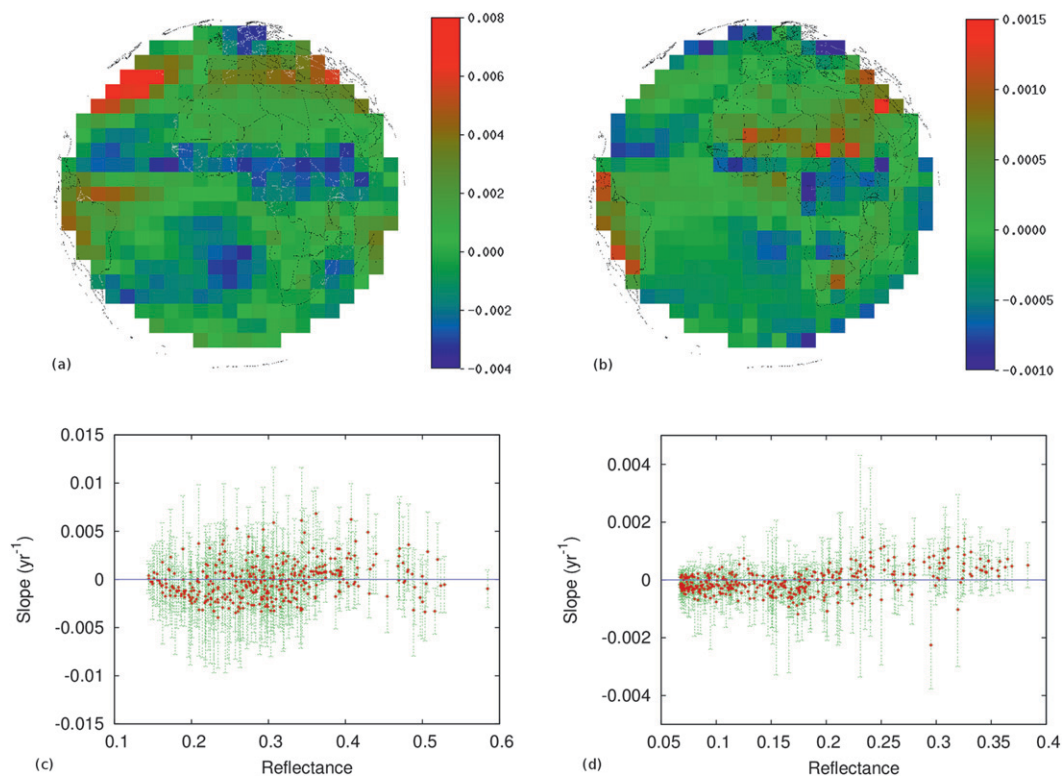


FIG. 8. Results of the regional validation method. (a) Spatial distribution of residual slope using the original images. (b) Spatial distribution of residual slope using the clear-sky images. (c) Residual slope as a function of mean reflectance using the original images. (d) Residual slope as a function of mean reflectance using the clear-sky images. Note that the range of the slopes is different in all figures. For the validation using the original images, the slopes have a larger range because of the presence of clouds than for the validation using the clear-sky images.

extreme positive values going as high as 0.007. From Fig. 8a it can be seen that these positive values are situated in the North Atlantic Ocean. The cloud fraction of MODIS for 2000–06 shows that in this region, there has been an increase in cloudiness over the years. An increasing amount of clouds explains the increasing reflectance, and thus the positive slope for this area. The standard deviation σ of the slopes is about 0.0015 yr^{-1} , so 95% of the boxes have a slope between -0.003 (-2σ) and 0.003 yr^{-1} (2σ); using an average radiance of 100 W m^{-2} , this results in stability of $3 \text{ W m}^{-2} \text{ decade}^{-1}$.

The same procedure is now applied on the composite clear-sky images (still using the all-sky simulations). For comparison, Fig. 8b shows the spatial distribution of the residual slopes for all boxes, while Fig. 8d gives the slope as a function of their mean reflectance, where each box still consists of 200×200 pixels. As the model is based on these clear-sky images, it is obvious that the results are better with smaller error bars. The few slopes with large errors come from parts of the FOV with permanent stratocumulus clouds, where it was not possible following our procedure to totally remove the presence

of clouds (e.g., in the Atlantic Ocean close to the west coast of Africa). To compare with the validation on the original images, the deviation of the slopes σ is smaller here (about $3.3 \times 10^{-4} \text{ yr}^{-1}$). With about 95% of the boxes with a slope between -6.6×10^{-4} (-2σ) and $6.6 \times 10^{-4} \text{ yr}^{-1}$ (2σ), the stability is about $0.66 \text{ W m}^{-2} \text{ decade}^{-1}$.

b. IGBP surface-type selection

In another validation step, the 17-class land cover dataset created by the IGBP Data and Information System is used. Based on these different surface types, 17 time series are created, where all pixels with the same surface type are spatially averaged into one time series. After the data are corrected using the spectral model and the optimal set of model parameters as given in Table 2, a linear fit is done for these 17 time series. The residual slope and the χ_{red} [using Eq. (8)] of the fits are given in Table 3. As no correction has been done for snowy surfaces in the Meteosat FOV by our model, surface type 15 is left out. The residual slopes are all smaller than their reduced chi-square statistics and are thus all within the

TABLE 3. For each IGBP surface type, its number is given, the name of the type, the slope per year of the fit through the spatial averaged time series for all pixels with this surface type, and the χ_{red} of the fit.

No.	Name	Sites in FOV (%)	Slope (yr^{-1})	χ_{red}
1	Evergreen needleleaf forest	0.505	2.5×10^{-4}	9.35×10^{-3}
2	Evergreen broadleaf forest	0.440	4.0×10^{-6}	1.40×10^{-3}
3	Deciduous needleleaf forest	0.003	1.3×10^{-4}	2.37×10^{-2}
4	Deciduous broadleaf forest	0.250	1.3×10^{-5}	1.41×10^{-3}
5	Mixed forest	0.146	1.2×10^{-4}	2.94×10^{-3}
6	Closed shrublands	0.763	-3.0×10^{-6}	1.04×10^{-3}
7	Open shrublands	2.874	3.9×10^{-5}	9.23×10^{-4}
8	Woody savannas	4.162	-1.3×10^{-5}	1.49×10^{-3}
9	Savannas	5.698	1.6×10^{-5}	1.07×10^{-3}
10	Grassland	2.262	5.4×10^{-5}	1.42×10^{-3}
11	Permanent wetlands	0.070	1.9×10^{-4}	3.51×10^{-3}
12	Croplands	2.273	1.2×10^{-5}	1.77×10^{-3}
13	Urban and built-up	0.021	1.4×10^{-5}	1.64×10^{-3}
14	Cropland mosaics	4.415	3.3×10^{-5}	1.01×10^{-3}
16	Bare soil and rocks	9.601	3.0×10^{-5}	1.14×10^{-3}
17	Water bodies	62.26	-3.0×10^{-6}	8.57×10^{-4}

uncertainty of the method close to zero. For surface types 1, 3, and 11, the χ_{red} is much higher than for the others because of the small sampling within the FOV (see % of sites in FOV for each IGBP class in Table 3).

c. Comparison with EUMETSAT model

A comparison is also carried out between the results of this model and the results of the model provided by EUMETSAT (Govaerts et al. 2004). Figure 6c shows the same six clear-sky and cloudy time series that were used to create our model; however, instead of correcting them for aging following the model explained in this paper and keeping the calibration coefficient constant, the model of EUMETSAT is used, where the calibration coefficient changes linearly in time, written as

$$C_f(t) = C_f + (D_f N_t 10^{-5})$$

with C_f the fixed calibration coefficient at launch ($=0.9184 \text{ W m}^{-2} \text{ sr}^{-1} \text{ DC}^{-1}$ for *Meteosat-7*), D_f as the daily drift ($=5.3507 \times 10^{-5} \text{ W m}^{-2} \text{ sr}^{-1} \text{ DC}^{-1} \text{ day}^{-1}$ for *Meteosat-7*), and N_t as the number of days since the date of launch. In Fig. 6c, it can be seen that the ocean and cloud time series are still decreasing, while the vegetation and desert time series are flat. The latter is as expected, as the desert targets were used in the vicarious calibration in the SSCC method. The fact that the wavelength dependency in the degradation was not taken into account in this model explains why not all time series have a zero slope.

6. Conclusions and future work

A spectral degradation was observed in the data of the *Meteosat* First Generation instrument *Meteosat-7*. To

correct for this, an aging model was created using three parameters. Validation shows that the model is working well for this satellite. With a stability of $0.66 \text{ W m}^{-2} \text{ decade}^{-1}$ on the clear-sky images, we are not that far off from the GCOS requirement of $0.2 \text{ W m}^{-2} \text{ decade}^{-1}$, so the idea of using a model including a wavelength dependency in the degradation seems to be consolidated. It is probably not possible to derive a more accurate model of spectral response degradation at this moment without having measurements of the spectra of the surface types.

Preliminary work has shown promising results for the rest of the MFG database. Once the full dataset is corrected for degradation, there is the possibility to create FCDRs from this. The main application in mind is to create top-of-atmosphere earth radiation budget through GERB-like data, and thus extending the GERB data records prior to its launch (Clerbaux et al. 2007). The modeled spectral response curve could also immediately be used to derive TCDRs for aerosol radiative forcing, aerosol optical depth, and surface albedo. Another option is that, instead of creating broadband data, the dataset could also be corrected based on, for example, the *Meteosat-7* spectral response curve at launch. This would lead to a full corrected narrowband dataset that might be more useful for applications where full corrected time series are needed, instead of just the modeled spectral response curve.

Acknowledgments. The authors would like to say thanks for the program LibRadtran, used for modeling cloudy radiances, and SBDART, for creating the simulations for the narrowband-to-broadband conversion in this work. Many thanks also go to Yves Govaerts,

Kory J. Priestley from the NASA Langley Research Center (VA), and Mark E. Frink from Northrop Grumman (CA) for providing more insight into the work. This research was supported by the Climate Monitoring Satellite Application Facility (CM SAF) of EUMETSAT.

REFERENCES

- Baldrige, A. M., S. J. Hook, C. I. Grove, and G. Rivera, 2009: The ASTER spectral library version 2.0. *Remote Sens. Environ.*, **113**, 711–715.
- Bertrand, C., N. Clerbaux, A. Ipe, S. Dewitte, and L. Gonzalez, 2006: Angular distribution models anisotropic correction factors and sun glint: A sensitivity study. *Int. J. Remote Sens.*, **27**, 1741–1757.
- Brooks, D. R., C. F. England, G. E. Hunt, and P. Minnis, 1984: An intercalibration of Meteosat-1 and GOES-2 visible and infrared measurements. *J. Atmos. Oceanic Technol.*, **1**, 283–286.
- Clerbaux, N., S. Dewitte, C. Bertrand, D. Caprion, B. De Paepe, L. Gonzalez, and A. Ipe, 2007: GERB-like data from Meteosat First Generation. [Available online at http://www.eumetsat.int/home/Main/AboutEUMETSAT/Publications/ConferenceandWorkshopProceedings/2007/groups/cps/documents/document/pdf_conf_p50_s10_06_clerbaux_p.pdf]
- , and Coauthors, 2008: Unfiltering of the Geostationary Earth Radiation Budget (GERB) data. Part I: Shortwave radiation. *J. Atmos. Oceanic Technol.*, **25**, 1087–1105.
- Delwart, S., R. Preusker, L. Bourq, R. Santer, D. Ramon, and J. Fischer, 2006: MERIS in-flight spectral calibration. *Proc. Second Working Meeting on MERIS and AATSR Calibration and Geophysical Validation (MAVT-2006)*, Frascati, Italy, European Space Agency. [Available online at http://envisat.esa.int/workshops/mavt_2006/papers/60_delwa.pdf]
- Doelling, D. R., L. Nguyen, and P. Minnis, 2004a: Calibration comparisons between SEVIRI, MODIS and GOES data. *Proc. EUMETSAT Meteorological Satellite Conf.*, Prague, Czech Republic, EUMETSAT, 77–83.
- , —, and —, 2004b: On the use of deep convective clouds to calibrate AVHRR data. *Earth Observing Systems IX*, W. L. Barnes and J. J. Butler, Eds., International Society for Optical Engineering (SPIE Proceedings, Vol. 5542), doi:10.1117/12.560047.
- Doelling, D., and M. M. Finckenor, 1999: Material selection guidelines to limit atomic oxygen effects on spacecraft surfaces. NASA Tech. Publ. NASA/TP-1999-209260, 50 pp.
- Dozier, J., 1989: Spectral signature of Alpine snow cover from the Landsat Thematic Mapper. *Remote Sens. Environ.*, **28**, 9–22.
- Eidenshink, J. C., and J. L. Faundeen, 1994: The 1 km AVHRR global land data set: First stages in implementation. *Int. J. Remote Sens.*, **15**, 3443–3462.
- Frink, M., M. Folkman, and L. Darnton, 1992: Photodeposition of molecular contaminants with a vacuum ultraviolet solar illumination lamp. *Optical System Contamination: Effects, Measurement, Control III*, A. P. M. Glassford, Ed., International Society for Optical Engineering (SPIE Proceedings, Vol. 1754), 46–57.
- Goldberg, M., and Coauthors, 2011: The Global Space-Based Inter-Calibration System. *Bull. Amer. Meteor. Soc.*, **92**, 467–475.
- Govaerts, Y. M., A. Arriaga, and J. Schmetz, 2001: Operational vicarious calibration of the MSG/SEVIRI solar channels. *Adv. Space Res.*, **28**, 21–30.
- , M. Clerici, and N. Clerbaux, 2004: Operational calibration of the Meteosat radiometer VIS band. *IEEE Trans. Geosci. Remote Sens.*, **42**, 1900–1914.
- Gube, M., V. Gärtner, and J. Schmetz, 1996: Analysis of the operational calibration of the Meteosat infrared-window channel. *Meteor. Appl.*, **3**, 307–316.
- Ipe, A., N. Clerbaux, C. Bertrand, S. Dewitte, and L. Gonzalez, 2003: Pixel-scale composite top-of-the-atmosphere clear-sky reflectances for Meteosat-7 visible data. *J. Geophys. Res.*, **108**, 4612, doi:10.1029/2002JD002771.
- Key, J. R., P. Yang, B. A. Baum, and S. L. Nasiri, 2002: Parameterization of shortwave ice cloud optical properties for various particle habits. *J. Geophys. Res.*, **107**, 4181, doi:10.1029/2001JD000742.
- Koepke, P., 1982: Vicarious satellite calibration in the solar spectral range by means of calculated radiances and its application to Meteosat. *Appl. Opt.*, **21**, 2845–2854.
- Kriebel, K.-T., and V. Amann, 1993: Vicarious calibration of the Meteosat visible channel. *J. Atmos. Oceanic Technol.*, **10**, 225–232.
- Kummerow, C., W. Barnes, T. Kozu, J. Shiue, and J. Simpson, 1998: The Tropical Rainfall Measuring Mission (TRMM) sensor package. *J. Atmos. Oceanic Technol.*, **15**, 809–817.
- Lefèvre, M., O. Bauer, A. Lehle, and L. Wald, 2000: An automatic method for the calibration of time-series of Meteosat images. *Int. J. Remote Sens.*, **21**, 1025–1045.
- Loeb, N. G., N. Manalo-Smith, S. Kato, W. F. Miller, S. K. Gupta, P. Minnis, and B. A. Wieliki, 2003: Angular distribution models for top-of-atmosphere radiative flux estimation from the Clouds and the Earth's Radiant Energy System instrument on the Tropical Rainfall Measuring Mission satellite. Part I: Methodology. *J. Appl. Meteor.*, **42**, 240–265.
- Loveland, T. R., and A. S. Belward, 1997: The IGBP-DIS global 1km land cover data set, DISCover: First results. *Int. J. Remote Sens.*, **18**, 3289–3295.
- Matthews, G., K. J. Priestley, P. Spence, D. Cooper, and D. Walikainen, 2005: Compensation for spectral darkening of short wave optics occurring on the Cloud's and the Earth's Radiant Energy System. *Earth Observing Systems X*, J. J. Butler, Ed., International Society for Optical Engineering (SPIE Proceedings, Vol. 5882), doi:10.1117/12.618972.
- Mayer, B., and A. Kylling, 2005: Technical note: The libRadtran software package for radiative transfer calculations - Description and examples of use. *Atmos. Chem. Phys. Discuss.*, **5**, 1319–1381.
- Moulin, C., C. E. Lambert, J. Poitou, and F. Dulac, 1996: Long term (1983-1994) calibration of the Meteosat solar (VIS) channel using desert and ocean targets. *Int. J. Remote Sens.*, **17**, 1183–1200.
- Powell, M. J. D., 1964: An efficient method for finding the minimum of a function of several variables without calculating derivatives. *Comput. J.*, **7**, 155–162.
- Qian, C., C. Fu, and Z. Wu, 2011: Changes in the amplitude of the temperature annual cycle in China and their implication for climate change research. *J. Climate*, **24**, 5292–5302.
- Ricchiazzi, P., S. Yang, C. Gautier, and D. Soble, 1998: SBDART: A research and teaching software tool for plane-parallel radiative transfer in the earth's atmosphere. *Bull. Amer. Meteor. Soc.*, **79**, 2101–2114.
- Rigollier, C., M. Lefèvre, P. Blanc, and L. Wald, 2002: The operational calibration of images taken in the visible channel of the Meteosat series of satellites. *J. Atmos. Oceanic Technol.*, **19**, 1285–1293.
- Sohn, B. J., J. Schmetz, S. Tjemkes, M. Koenig, H. Lutz, A. Arriaga, and E. S. Chung, 2000: Intercalibration of the Meteosat-7 water

- vapor channel with SSM/T-2. *J. Geophys. Res.*, **105** (D12), 15 673–15 680.
- Stewart, T. B., G. S. Arnold, D. F. Hall, D. C. Marvin, W. C. Hwang, R. C. Y. Owl, and H. D. Marten, 1990: Photochemical spacecraft self-contamination: Laboratory results and systems impacts. Aerospace Rep. TOR-0090(5470-01)-3, The Aerospace Corporation, 42 pp.
- Szekiela, K.-H., 1988: *Satellite Monitoring of the Earth*. Wiley and Sons, 326 pp.
- Tjemkes, S. A., M. König, H.-J. Lutz, L. C. J. van de Berg, and J. Schmetz, 2001: Calibration of Meteosat water vapor channel observations with independent satellite observations. *J. Geophys. Res.*, **106** (D6), 5199–5209.
- Tribble, A. C., B. Boyadjian, J. Davis, J. Haffner, and E. McCullough, 1996: Contamination control engineering design guidelines for the aerospace community. NASA Contractor Rep. 4740, Rockwell International Corporation, 126 pp.
- van de Berg, L. C. J., J. Schmetz, and J. Whitlock, 1995: On the calibration of the Meteosat water vapor channel. *J. Geophys. Res.*, **100** (D10), 21 069–21 076.
- Vermote, E., and Y. J. Kaufman, 1995: Absolute calibration of AVHRR visible and near-infrared channels using ocean and cloud views. *Int. J. Remote Sens.*, **16**, 2317–2340.
- Wielicki, B. A., B. R. Barkstrom, E. F. Harrison, R. B. Lee III, G. L. Smith, and J. E. Cooper, 1996: Clouds and the Earth's Radiant Energy System (CERES): An Earth Observing System experiment. *Bull. Amer. Meteor. Soc.*, **77**, 853–868.
- WMO, 2006: Systematic observation requirements for satellite-based products for climate. GCOS-107, WMO/TD-1338, 90 pp.
- Xiong, X., R. E. Eplee Jr., J. Sun, F. S. Patt, A. Angal, and C. R. McClain, 2009: Characterization of MODIS and SeaWiFS solar diffuser on-orbit degradation. *Earth Observing Systems XIV*, J. J. Butler, X. Xiong, and X. Gu, Eds., International Society for Optical Engineering (SPIE Proceedings, Vol. 7452), doi:10.1117/12.824797.
- Yang, S., F. Weng, B. Yan, N. Sun, and M. Goldberg, 2011: Special Sensor Microwave Imager (SSM/I) intersensor calibration using a simultaneous conical overpass technique. *J. Appl. Meteor. Climatol.*, **50**, 77–95.